Full-Wave Space-Domain Analysis of Open Microstrip Discontinuities Including the Singular Current-Edge Behavior

Jeannick Sercu, Niels Faché, Frank Libbrecht, and Daniël De Zutter, *Member, IEEE*

Abstract—**A full-wave space-domain analysis is presented for the high-frequency characterization of microstrip discontinuities. This approach solves the electric field integral equation (EFIE) for the surface current density on the microstrip using the method of moments. The current expansion functions incorporate the singular edge behavior of the surface current, yielding a very accurate current modeling. Special attention is devoted to the analytical treatment of the singular terms in the electric field Green's dyadic. The numerical results focus on the S-parameters of some simple microstrip discontinuities and the comparison with results obtained with other techniques and from measurements.**

I. Introduction

MIC and MMIC designers rely highly on microwave CAD tools to reduce the design cycles of microwave integrated circuits. In modern and future high-speed digital systems, high-frequency effects play an important role, as the integration density increases and bandwidths become larger (bit rates of 150 Mb/s and more). Degradation of signals transported along microstrip interconnection lines is not only caused by the inherent dispersion characteristics of the microstrip lines, but is also influenced by the reactive (evanescent higher order modes) and resistive (radiation of surface and space waves) effects that occur at line discontinuities (step-in-width, bend, T-junction, etc.).

Microstrip discontinuities, together with microstrip line segments are the basic elements of microstrip integrated circuits. In order to provide the designers with a CAD tool that accurately predicts the electromagnetic behavior of microwave circuits (filters, couplers, resonators, etc.), an accurate high-frequency characterization of these discontinuities by means of a rigorous full-wave analysis is required. Full-wave analysis techniques for microstrip discontinuities are proposed and discussed in a large body of technical literature [2]–[4] [7]–[15]. In time-domain analysis, several numerical schemes can be used, however the finite-difference time-domain method (FDTD) is by far the most popular one [7], [11], [14]. The major drawbacks of the FDTD technique are the imperfection of the absorbing boundary condition and the large memory and CPU-time requirements.

Manuscript received September 25, 1992; revised February 10, 1993.

The authors are with the Laboratory of Elektromagnetism and Acoustics, University of Ghent, 9000 Gent, Belgium.

IEEE Log Number 9211856.

In the frequency domain, the integral equation method provides very versatile method-of moment techniques for characterizing microstrip planar structures. The electromagnetic behavior of the planar circuit is described by either a mixed potential integral equation (MPIE) for the surface current and charge [4] or an electric field integral equation (EFIE) for the current [2], [12], [15]. The planar circuit is divided into rectangular and/or triangular cells. Subsectional basis functions are used in the expansion of the two unknown current components. The charge is derived from the current. From the solution of the integral equation follows the current and the S parameters of the circuit under study.

The elements of the impedance matrix of the discretized integral equation can either be calculated in the spectral domain or in the spatial domain. The spectral domain approach is very efficient for microstrip structures on a substrate enclosed in a box when a uniform grid is used. In that case special approaches based on FFT techniques can be used [3], [10], [13]. However, the accuracy of the results is often influenced by the presence of box resonances and radiation losses can only be taken into account approximately, by modeling the top cover of the box as a surface impedance wall of 377 Ω/s. These losses sometimes play an important role in the degradation of the circuit performance.

A powerful advantage of the spatial-domain approach is the possibility to precalculate the Green's dyadic and store the results in a database. The spatial-domain Green's dyadic only depends on the characteristics of the layered medium in which the planar structure is embedded, not on the geometry of the planar structure itself. Since the microwave designer will not often change the technology and hence the layered medium, but will optimize the circuit performance by making small changes to the geometry of the planar structure, it is obvious that the spatial-domain Green's dyadic database approach makes the technique very efficient for microwave CAD applications.

The approach presented in this paper is based on the electric field integral equation for the surface current and uses such a database technique for the spatial domain Green's dyadic. The derivation of the relevant electric field Green's dyadic suited for this purpose has been presented elsewhere [6]. The EFIE is solved by the method of moments. The surface current is expanded into bilinear basis functions in the nonboundary cells of the grid and into special functions in the corner and edge cells. The latter functions take the well-known square root edge

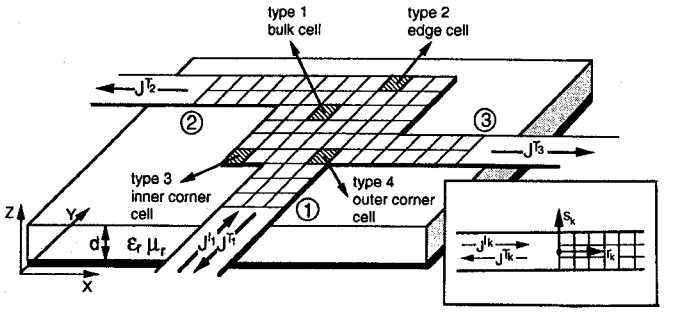

Fig. 1. A general N-port microstrip discontinuity with connecting feedlines L_k $(k = 1, \cdots, 3)$ and single-port excitation. A rectangular grid is used to subdivide the microstrip discontinuity. The inset shows the local coordinate system associated with each feedline.

behavior into account [1], [5]. This results in a very accurate current modeling. The circuit is excited by the fundamental mode propagating on each port transmission line. The integral equation is tested with pulse functions. In contradistinction to other spatial techniques, the elements of the impedance matrix are calculated starting from the electric field Green's dyadic kernel. Special attention is devoted to the analytical treatment of the singular terms which occur in the electric field Green's dyadic.

The numerical results focus on the S parameters of some simple microstrip discontinuities for which published results exist. As will be shown, the results obtained with our simulation technique agree very well with the simulation results obtained with other techniques and with experimental data found in literature. A detailed error analysis of the comparison with the experimental results is not included, since no error bars were provided by the authors of the experimental data.

II. General Formulations

A general N-port microstrip discontinuity is shown in Fig. 1. It consists of a discontinuity region together with N connecting feedlines L_k $(k = 1, \cdots, N)$. Part of the lines is taken up into the discontinuity, accounting for the reactive effects of the evanescent higher order modes near the feedline-discontinuity junction. Outside this region, it is assumed that the connecting lines only propagate the lowest order fundamental eigenmode.

The microstrip structure is excited at its ports with the incoming fields associated with the fundamental eigenmode. The incoming currents $\boldsymbol{J}^{I_k}(\boldsymbol{r})$ $(k = 1, \cdots, N)$ are scattered at the microstrip discontinuity and outcoming (reflected and/or transmitted) currents $\boldsymbol{J}^{T_k}(\boldsymbol{r})$ $(k = 1, \cdots, N)$ propagate along the feedlines. The calculation of these currents yields the normalized S parameters of the N-port microstrip discontinuity. Renormalization of the S parameters to 50 Ω, or any other desired value, makes them suitable for use in microwave CAD applications.

The associated electromagnetic field problem is described by an electric field integral equation (EFIE) for the surface current density, which follows form imposing the boundary condition, i.e., the zero tangential electric field on the microstrip surface $(z = d)$. This leads to

$$\lim_{z \to d} \int\int_S \left[G^E_{xx}(\boldsymbol{r}, \boldsymbol{r}') J_x(\boldsymbol{r}') + G^E_{xy}(\boldsymbol{r}, \boldsymbol{r}') J_y(\boldsymbol{r}') \right] dS' = -E^{in}_x(\boldsymbol{r})$$

$$\lim_{z \to d} \int\int_S \left[G^E_{yx}(\boldsymbol{r}, \boldsymbol{r}') J_x(\boldsymbol{r}') + G^E_{yy}(\boldsymbol{r}, \boldsymbol{r}') J_y(\boldsymbol{r}') \right] dS' = -E^{in}_y(\boldsymbol{r}) \tag{1}$$

where E^{in} is the excitation field associated with the incoming currents. Strictly speaking, (1) is obtained from a limiting process in which the observation point r approaches the planar structure located in the plane $z = d$ from outside this plane. We have carefully retained this limiting operation outside the integration as this will be important in the sequel.

The kernel of (1) is the space-domain electric field Green's dyadic $\boldsymbol{G}^E(\boldsymbol{r}, \boldsymbol{r}')$ of the layered medium in which the planar circuit is embedded. The EFIE is solved using the method of moments. The microstrip discontinuity is gridded up into a finite number of uniform rectangular subsections or cells S_j (as shown in Fig. 1). The surface current is modeled with subsectional basis functions $\{b_{\beta,j}(\boldsymbol{r}), \beta = x, y, j = 1, \cdots, M\}$ described in Section III. The incoming and outcoming currents on the $k$the feedline are given by

$$\boldsymbol{J}^{I_k}(\boldsymbol{r}) = j_k(s_k) e^{-j\beta_k r_k} \boldsymbol{u}_{r_k}$$
$$\boldsymbol{J}^{T_k}(\boldsymbol{r}) = -T_k j_k(s_k) e^{j\beta_k r_k} \boldsymbol{u}_{r_k}. \tag{2}$$

In (2), (r_k, s_k) is a local coordinate system associated with the kth feedline, $j_k(s_k)$ and β_k are the transverse current dependence and propagation constant of the lowest order eigenmode and T_k is the unknown current reflection or transmission coefficient. The propagation constant is calculated using an analytical formula [16]. The current profile in the transverse direction is approximated by the Maxwell distribution (3). Only the longitudinal current component of the incoming mode is considered on the feedline as the transversal component is an order of magnitude smaller:

$$j_k(s_k) = \frac{2}{W_k \pi} \frac{1}{\sqrt{1 - \left(\frac{2s_k}{W_k}\right)^2}}. \tag{3}$$

The EFIE is tested with a set of M subsectional pulse functions $\{t_{\alpha,i}(\boldsymbol{r}) = 1, \alpha = x, y, i = 1, \cdots, M\}$, yielding a system of M linear equations, in the M unknown current expansion coefficients and N unknown reflection/transmission coefficients. The extra N equations, necessary to solve the problem, are obtained by imposing the continuity of the total longitudinal current across the joint boundary of the discontinuity region and each connected feedline L_k, $k = 1, \cdots, N$. The latter equations are referred to as the line-matching equations. The integral equation (1) is transformed into the following matrix equation:

$$\begin{bmatrix} [Z^{xx}_{ij}] & [Z^{xy}_{ij}] & [Z^{xT}_{ik}] \\ [Z^{yx}_{ij}] & [Z^{yy}_{ij}] & [Z^{yT}_{ik}] \\ [Z^{Mx}_{lj}] & [Z^{My}_{lj}] & [Z^{MT}_{lk}] \end{bmatrix} \begin{bmatrix} [I^x_j] \\ [I^y_j] \\ [T_k] \end{bmatrix} = \begin{bmatrix} [V^x_i] \\ [V^y_i] \\ [V^M_l] \end{bmatrix} \tag{4}$$

where the indices i and j range over all the gridcells $1, \cdots, M$ and the indices k and l range over all the feedlines $1, \cdots, N$. The first two sets of rows in (4) follow from the testing of the EFIE, while the last set of rows (indicated with the superscript M) results form the line-matching equations. The coefficients of the latter equations are easily calculated analytically. The elements of the submatrices $\left[Z^{\alpha\beta}\right]$ $(\alpha, \beta = x, y)$ describe the coupling between an excitation cell S_j with current basis function $b_{\beta,j}(\boldsymbol{r})$ and an observation cell S_i with associated test function $t_{\alpha,i}(\boldsymbol{r})$. The calculation of these cell-cell coupling elements will be discussed in Section IV where special attention is paid to the Green's functions singularities.

III. Current Modeling

For the purpose of this paper, we have chosen a uniform grid of rectangular subsections to grid up the discontinuity region, as illustrated in Fig. 1. The elementary dimensions of each cell are D_x and D_y. Taking the symmetry properties of such a grid into account, together with the translational invariance of the layered medium in the lateral (x, y) plane, we can speed up the calculations of the Z-matrix elements significantly.

We distinguish four types of grid cells, as shown in Fig. 1, depending on their position relative to the boundary of the planar structure. In a bulk cell (cell type 1), we use a bilinear expansion function (equation (5a)) to model both components of the current (see Fig. 2(a)). This basis function is modified for the boundary cells to incorporate the singular behavior of the current near the edge of the microstrip. This edge condition, described by Meixner [1], implies that the component of the current parallel to the edge becomes singular as $1/\sqrt{d}$, while the transversal component of the current goes to zero as $\sqrt{d}$, d being the distance to the edge. The current basis functions (equation (5b)) for edge cells (cell type 2) takes this edge behavior into account, as illustrated in Fig. 2(b).

The modeling of the current in the corner cells (cell types 3 and 4) is chosen such that the square root dependencies of both longitudinal and transversal components are matched, without violating the current continuity condition, i.e., current must be continuous in the direction of current flow. For an inner corner cell, the current basis function (equation (5c)) is given by simply taking the product of both square root dependencies as illustrated in Fig. 2(c). For an outer corner cell, the matching is achieved with the use of the special shape function $g(x, y)$ on which the square root dependencies (equation (5d)) are superimposed. Fig. 2(d) shows the basis functions used for an outer corner cell and Fig. 3 shows the special shape function $g(x, y)$.

$$b_x(x, y) = b_y(x, y) = \left(1 - \frac{x}{D_x}\right)\left(1 - \frac{y}{D_y}\right) \tag{5a}$$

$$\begin{aligned} b_x(x, t) &= \left(1 - \frac{x}{D_x}\right)\left(1 - \frac{y}{D_y}\right)^{-1/2} \\ b_y(x, y) &= \left(1 - \frac{x}{D_x}\right)\left(1 - \frac{y}{D_y}\right)^{1/2} \end{aligned} \tag{5b}$$

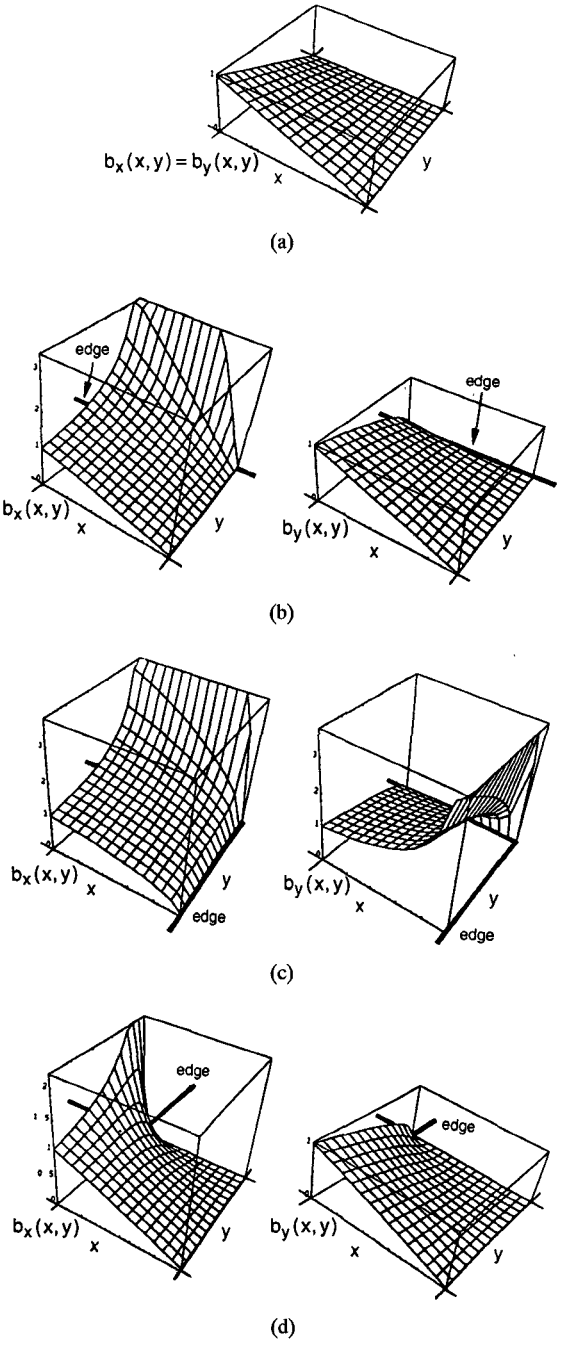

Fig. 2. The current expansion functions for the four types of grid cells. (a) Bulk cell. (b) Edge cell. (c) Inner corner cell. (d) Outer corner cell.

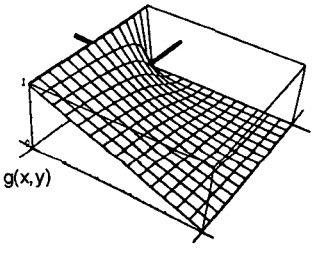

Fig. 3. Special shape function $g(x, y)$ used to match the square root dependencies of the current components in an outer corner cell.

$$b_x(x,y) = \left(1-\frac{x}{D_x}\right)^{1/2}\left(1-\frac{y}{D_y}\right)^{-1/2}$$
$$b_y(x,y) = \left(1-\frac{x}{D_x}\right)^{-1/2}\left(1-\frac{y}{D_y}\right)^{1/2} \tag{5c}$$

$$b_x(x,y) = g(x,y)\left(1-\frac{y}{D_y}\right)^{-1/2}$$
$$b_y(x,y) = g(x,y)\left(1-\frac{y}{D_y}\right)^{1/2} \tag{5d}$$

$$g(x,y) = \left(1-\frac{x}{\sqrt{x^2+(D_y-y)^2}}\right) - \frac{x}{D_x} \cdot \frac{\left(1-\frac{D_x}{\sqrt{D_x^2+(D_y-y)^2}}\right)\left(1-\frac{D_x}{\sqrt{x^2+D_y^2}}\right)}{\left(1-\frac{D_x}{\sqrt{D_x^2+D_y^2}}\right)}. \tag{6}$$

IV. Evaluation of the Cell–Cell Coupling Elements

The calculation of the Z-matrix elements is crucial to the solution of the EFIE. The general form of these elements is

$$Z_{ij}^{\alpha\beta} = \lim_{z\to d}\int\int_{S_i} dS\, t_{\alpha,i}(\boldsymbol{r})\int\int_{S_j} dS' \cdot G^E_{\alpha\beta}(\boldsymbol{r},\boldsymbol{r}')b_{\beta,j}(\boldsymbol{r}') \quad \alpha,\beta = x,y\,. \tag{7}$$

The two space-domain integrations over the observation and excitation cell can be carried out numerically for most of the cell–cell pairs, using simple Gaussian quadrature formulas. However, the elements for which the test and basis functions coincide (self-patch coupling) or overlap (nearest neighbor coupling) must be calculated analytically, in order to take the Green's dyadic singularities correctly into account.

In [6] it is shown that the electric field Green's dyadic can be derived from two scalar functions $W_0(\rho,z)$ and $W_2(\rho,z)$. The four tangential components needed in our simulation are given by

$$\begin{bmatrix} G^E_{xx} & G^E_{xy} \\ G^E_{yx} & G^E_{yy}\end{bmatrix} = \begin{bmatrix} W_0(\rho,z)-W_2(\rho,z)\cos 2\theta & -W_2(\rho,z)\sin 2\theta \\ -W_2(\rho,z)\sin 2\theta & W_0(\rho,z)+W_2(\rho,z)\cos 2\end{bmatrix} \tag{8}$$

where $\boldsymbol{r}-\boldsymbol{r}' = \rho(\cos\theta\boldsymbol{u}_x + \sin\theta\boldsymbol{u}_y) + (z-d)\boldsymbol{u}_z$. Polar coordinates (ρ,θ) are used to denote the lateral separation between the excitation and the observation point. The numerical procedure described in [6] makes the calculation of the Green's dyadic possible for layered structures with an arbitrary number of lossless and/or dielectric and magnetic layers.

In general, the Green's functions $W_0(\rho,z)$ and $W_2(\rho,z)$ exhibit a singularity for $\rho = 0$. This singular term is extracted analytically. The remaining regular parts, given as a Sommerfeld type of integral, are precalculated for a small number of ρ values and tabulated in a database. A second-order Lagrange interpolation scheme is used to retrieve the results from this database, for any value of ρ. A powerful advantage of this technique is the ability to model multilayered substrates by simply replacing the database for the single-layered Green's dyadic by the database for the multilayered Green's dyadic.

The general results in [6] for the singular parts of the $W_i(\rho,z)$ functions lead to

$$W_0^{\sin g}(\rho,z) = g_3\frac{\rho^2-2\delta^2}{(\rho^2+\delta^2)^{5/2}} + (g_2+g_1)\frac{1}{(\rho^2+\delta^2)^{1/2}}$$
$$W_2^{\sin g}(\rho,z) = g_3\frac{-3\rho^2}{(\rho^2+\delta^2)^{5/2}} + (g_2-g_1)\frac{\left[(\rho^2+\delta^2)^{1/2}-\delta\right]^2}{\rho^2(\rho^2+\delta^2)^{1/2}} \tag{9}$$

where

$$g_1 = -j\frac{\omega\mu_0}{4\pi}\frac{\mu_r}{1+\mu_r}$$
$$g_2 = -j\frac{\omega\mu_0}{4\pi}\frac{1+\varepsilon_r^2\mu_r}{2(1+\varepsilon_r)^2}$$
$$g_3 = -j\frac{1}{4\pi\omega\varepsilon_0}\frac{1}{1+\varepsilon_r}. \tag{10}$$

In (9) $\delta = z-d$ represents a small distance above the microstrip structure and g_1, g_2, and g_3 are complex coefficients depending only on the frequency and the complex relative permittivity and permeability of the microstrip substrate. The terms in (9) depending on g_3 give rise to a $1/\rho^3$ singularity, as δ goes to zero. The other terms give rise to a $1/\rho$ singularity.

The contribution to the cell–cell coupling associated with the regular part of the Green's dyadic presents no calculational difficulties and can easily be computed numerically. For the evaluation of the self-patch and nearest neighbor coupling terms, the contributions coming from the singular part must be calculated analytically. At this point however, it can be seen that it is not allowed to interchange the integrations in the self-patch and nearest neighbor integrals and the limiting process $\delta \to 0$, as this leads to divergent results for the $1/\rho^3$ singularity. In order to evaluate these integrals correctly, it is necessary to start form the values (9) with $\delta \neq 0$. One of the two space-domain integrations in (7) must be performed analytically at a small distance δ above the planar structure. It is obvious that the integration over the observation cell is performed first, as the simple pulse test functions are much easier to deal with than the current expansion functions. We therefore interchange the integration over the excitation cell with the integration over the observation cell. For the contribution of the singular part, expression (7) is

replaced by

$$Z_{ij}^{\alpha\beta,\sin g} = \int\int_{S_j} dS' b_{\beta,j}(\boldsymbol{r}') \cdot \left\{ \lim_{z\to d} \int\int_{S_i} dS G_{\alpha\beta}^{E,\sin g}(\boldsymbol{r},\boldsymbol{r}') t_{\alpha,i}(\boldsymbol{r}) \right\}. \quad (11)$$

The use of simple pulse test functions $\{t_{\alpha,i}(\boldsymbol{r}) = 1, \alpha = x, y, i = 1, \cdots, M\}$ allows the second integral in (11) to be calculated analytically with $\delta \neq 0$. After this step, the limit $\delta \to 0$ can be carried out, yielding a nondivergent excitation integral. Results of these calculations are given in the Appendix for an observation cell of general polygonal shape. In the final step, the excitation integral is calculated numerically using simple Gaussian quadrature formulas for the bulk cells and appropriate Gauss–Jacobi quadrature formulas for the boundary cells, taking the special square root edge behavior of the current basis functions into account.

V. Numerical Results

A. Microstrip Stub

The presented technique has been applied to characterize the microstrip stub configuration shown in the inset of Fig. 4(a). This structure is found in several publications [8], [9]. The microstrip single stub contains two discontinuities: a T-junction and an open end. It is printed on an alumina substrate with thickness $d = 1.27$ mm and relative dielectric constant $\varepsilon_r = 10.65$. The line width W and the stub length L are equal to 1.4 and 2.1 mm, respectively. Fig. 4(a) shows the phase and Fig. 4(b) the magnitude of the simulated S_{21} scattering parameter. Also included in the plot are the results from previously published data obtained with the spectral-domain technique [8] and from measurements [8]. As shown in Fig. 4, the agreement between our technique and the measurements is very good. The resonance frequency of the microstrip stub lays just beyond 10 GHz, which is predicted correctly by the simulation results.

The full-wave analysis presented in this paper includes all high-frequency effects such as coupling, radiation, and surface waves. Radiation losses form open microstrip circuits can be significant at microwave and millimeter-wave frequencies. To illustrate this radiation effect, Fig. 4(b) shows the quantity $G = |S_{11}|^2 + |S_{21}|^2$, which follows from the full-wave analysis. $(1 - G)$ represents the fraction of incident power lost in the microstrip discontinuity. For a lossless substrate, this power loss is totally due to radiation. The plot of G shows that in the considered frequency range, the calculated radiation loss reaches a peak of about 27% just below 11 GHz.

B. Microstrip Bend

The next example discussed here is the analysis of the microstrip bend discontinuity shown in Fig. 5. It was mainly chosen for further verification of our technique by comparison with measurements. The epoxy substrate has a thickness of $d = 1.6$ mm and a relative dielectric constant $\varepsilon_r = 4.5$. The width W of the microstrip is 3 mm. The magnitudes of

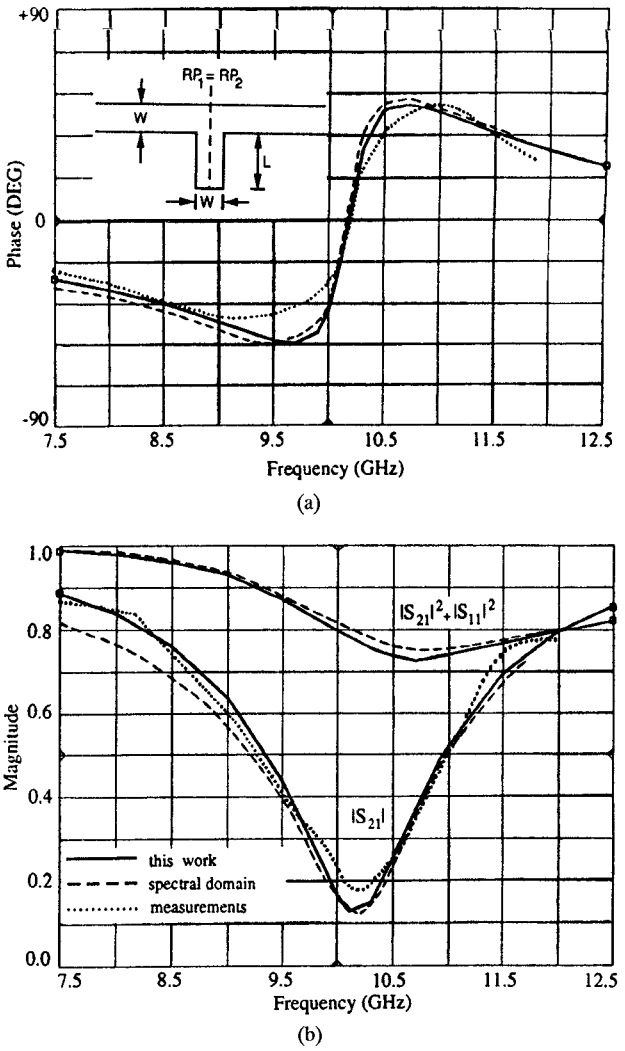

Fig. 4. Scattering parameters of a microstrip single stub calculated with the spatial and the spectral domain technique [8]. (a) Phase of S_{21}. (b) Magnitude of S_{21} and $|S_{11}|^2 + |S_{21}|^2$.

the scattering parameters S_{11} and S_{21} are shown in Fig. 5(a). The value of $G = |S_{11}|^2 + |S_{21}|^2$ is plotted in Fig. 5(b). The results are compared with published data calculated with the finite-difference time-domain technique [14] and with measurements [14]. Again the agreement with the experimental results is found to be very good, which validates the theoretical results. The oscillations in the experimental plots are due to the imperfect connector-strip transition. The difference between G and unity shows that at the considered frequencies, an important part of the incident power is radiated by the corner into space and surface waves.

C. Double-Loop Meander Line

The third example considers the double loop meander line configuration presented by Wertgen and Jansen [10]. The structure is printed on a 25-mil standard alumina substrate of measured relative dielectric constant $\varepsilon_r = 9.978$ with unknown precision, i.e., no $+/-$ tolerance is specified in [10]. The other relevant parameters are $W = 0.61$ mm, $S = W/2$, and $L = 4W$. Multiloop meander lines are frequently used in the design of traveling-wave FET amplifiers for their slow-

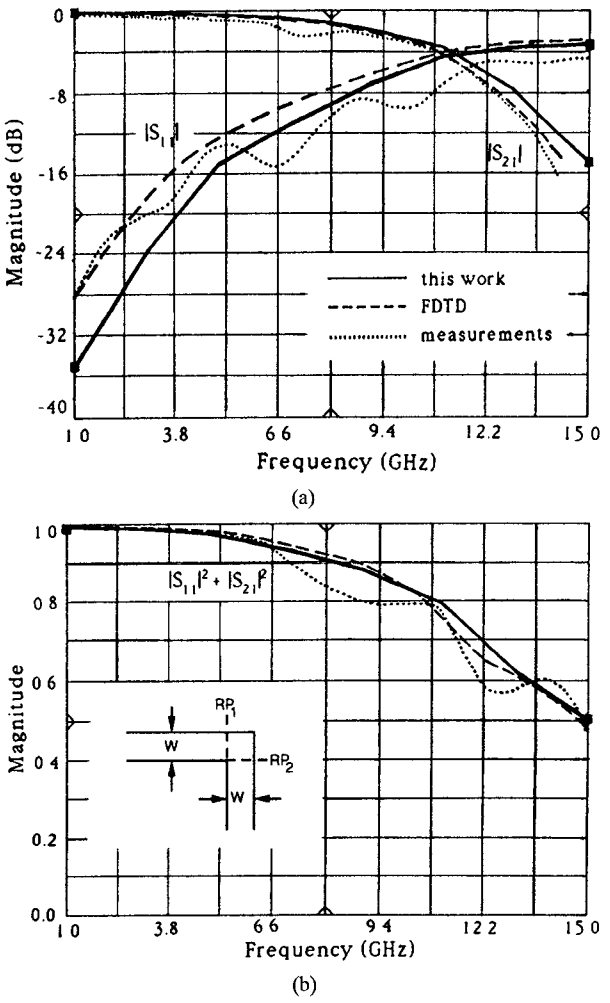

Fig. 5. Scattering parameters of a microstrip bend. (a) Magnitude of S_{11} and S_{21}. (b) Magnitude of $|S_{11}|^2 + |S_{21}|^2$.

wave properties. The meander line contains several tightly coupled 90° bends. The electromagnetic coupling between two bends, spaced by only half a substrate thickness or less, has a very important effect on the slow-wave properties of the structure.

The results of the numerical simulation are presented in Fig. 6(a)–(c). Also shown in Fig. 6 are theoretical results obtained with a closed-box spectral domain technique [10] and open experimental data [10]. The agreement between the numerical results and the experimental data is very good in the whole frequency range. In addition, it can be seen that the closed-box simulation results show some deviations form the measured plots, especially for frequencies beyond 11 GHz. These deviations are mainly due to the absence of radiation losses in the closed-box simulation technique. This is confirmed by the plot of $|S_{11}|^2+|S_{21}|^2$ (Fig. 6(c)). It shows that the power loss due to radiation becomes significant (>5%) for frequencies beyond 11 GHz.

VI. Conclusions

A full-wave space-domain technique has been presented for the simulation of the high-frequency S parameters of microstrip discontinuities. This technique is based on the

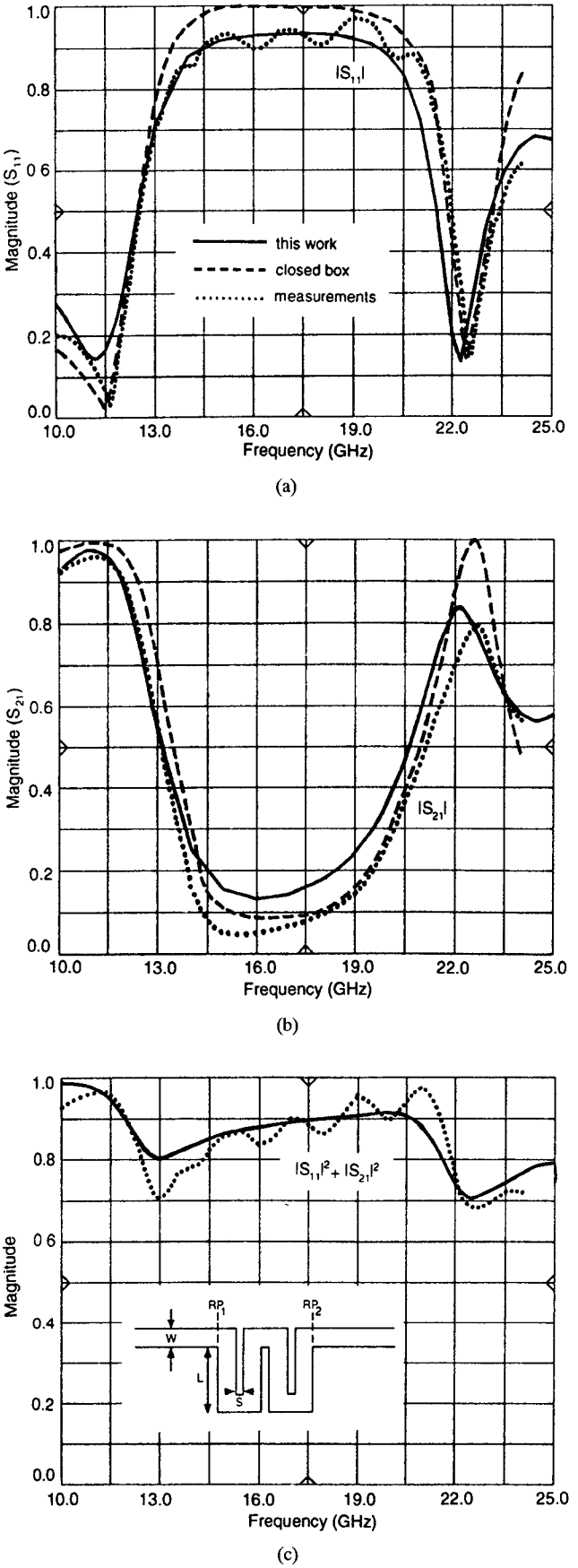

Fig. 6. Scattering parameters of a microstrip double loop meander line calculated with an open- and a closed-box simulation technique [10]. (a) Magnitude of S_{11}. (b) Magnitude of S_{21}. (c) Magnitude of $|S_{11}|^2 + |S_{21}|^2$.

electric field integral equation for the surface current on the microstrip structure. A suitable electric field Green's dyadic describes the layered medium in which the microstrip structure is embedded. The database approach of this Green's dyadic makes the technique very efficient.

To solve the integral equation, the method of moments was applied. A correct handling of the self-patch and nearest neighbor coupling was only possible starting from the analytical knowledge of the singular behavior of the Green's dyadic. The current basis functions, used to model the surface current density in the microstrip structure, incorporate the singular edge behavior of the current.

The numerical results focus on some simple microstrip discontinuities for which published results exist. The comparison of our results with the published data allowed the validation of the proposed technique. Future research will be focused on an extensive comparison of the current basis functions introduced in this paper (bilinear including the singular edge behavior) with the more traditional rooftop basis functions.

APPENDIX

The following integrals are involved in the calculation of the observation integrals (11):

$$
\begin{aligned}
A_{11}(\boldsymbol{r}') &= \int\!\!\int_{S_i} dS \frac{1}{\rho} \\
A_{12}(\boldsymbol{r}') &= (\boldsymbol{r}') = \int\!\!\int_{S_i} dS \frac{1}{\rho} \cos 2\theta \\
A_{13}(\boldsymbol{r}') &= \int\!\!\int_{S_i} dS \frac{1}{\rho} \sin 2\theta \\
A_{31}(\boldsymbol{r}') &= \lim_{\delta \to 0} \int\!\!\int_{S_i} dS \frac{\rho^2 - 2\delta^2}{(\rho^2 + \delta^2)^{5/2}} \\
A_{32}(\boldsymbol{r}') &= \lim_{\delta \to 0} \int\!\!\int_{S_i} dS \frac{\rho^2}{(\rho^2 + \delta^2)^{5/2}} \cos 2\theta \\
A_{33}(\boldsymbol{r}') &= \lim_{\delta \to 0} \int\!\!\int_{S_i} dS \frac{\rho^2}{(\rho^2 + \delta^2)^{5/2}} \sin 2\theta \,. \qquad \text{(A1)}
\end{aligned}
$$

The limiting operation $\delta \to 0$ has been carried out for the integrals of the first column, as the $1/\rho$ singularity can be integrated analytically over the observation cell. This however cannot be done for the integrals of the second column. The $1/\rho^3$ singularity is too strong to be integrated directly. The integrals in (A1) are calculated using the polar coordinates introduced in (8). The integration domain S_i (which can be of general polygonal shape) is divided into a finite number of oriented triangles $S_i^{(m)}$, as indicated in Fig. 7(a) for a general quadrangle.

The results of the integrations over the oriented triangle $S_i^{(m)}$ are given below. The relevant parameters of the oriented triangle $S_i^{(m)}$ used here are illustrated in Fig. 7(b). $L_0^{(m)}$ is the distance between r' and side m of the observation cell S_i.

$$
\begin{aligned}
A_{11}(\boldsymbol{r}') &= \sum_m \alpha_1^{(m)}(\boldsymbol{r}') \\
A_{12}(\boldsymbol{r}') &= \sum_m \Big[\Big(\alpha_2^{(m)}(\boldsymbol{r}') - \alpha_1^{(m)}(\boldsymbol{r}') \Big) \cos 2\theta_0^{(m)} \\
&\qquad - \alpha_3^{(m)}(\boldsymbol{r}') \sin 2\theta_0^{(m)} \Big] \\
A_{13}(\boldsymbol{r}') &= \sum_m \Big[\Big(\alpha_2^{(m)}(\boldsymbol{r}') - \alpha_1^{(m)}(\boldsymbol{r}') \Big) \sin 2\theta_0^{(m)} \\
&\qquad + \alpha_3^{(m)}(\boldsymbol{r}') \cos 2\theta_0^{(m)} \Big] \qquad \text{(A2)}
\end{aligned}
$$

with

$$
\begin{aligned}
\alpha_1^{(m)}(\boldsymbol{r}') &= L_0^{(m)} \\
&\quad \cdot \left[\frac{\cos\Big(\theta_1^{(m)} - \theta_0^{(m)}\Big)\Big(1 + \sin\Big(\theta_2^{(m)} - \theta_0^{(m)}\Big)\Big)}{\cos\Big(\theta_2^{(m)} - \theta_0^{(m)}\Big)\Big(1 + \sin\Big(\theta_1^{(m)} - \theta_0^{(m)}\Big)\Big)} \right] \\
\alpha_2^{(m)}(\boldsymbol{r}') &= 2L_0^{(m)} \\
&\quad \cdot \Big[\sin\Big(\theta_2^{(m)} - \theta_0^{(m)}\Big) - \sin\Big(\theta_1^{(m)} - \theta_0^{(m)}\Big) \Big] \\
\alpha_3^{(m)}(\boldsymbol{r}') &= -2L_0^{(m)} \\
&\quad \cdot \Big[\cos\Big(\theta_2^{(m)} - \theta_0^{(m)}\Big) - \cos\Big(\theta_1^{(m)} - \theta_0^{(m)}\Big) \Big] \qquad \text{(A3)}
\end{aligned}
$$

$$
\begin{aligned}
A_{31}(\boldsymbol{r}') &= \sum_m \beta_1^{(m)}(\boldsymbol{r}') \\
A_{32}(\boldsymbol{r}') &= \sum_m \Big[\Big(\beta_2^{(m)}(\boldsymbol{r}') + \beta_1^{(m)}(\boldsymbol{r}') \Big) \sin 2\theta_0^{(m)} \\
&\qquad - \beta_3^{(m)}(\boldsymbol{r}') \sin 2\theta_0^{(m)} \Big] \\
A_{33}(\boldsymbol{r}') &= \sum_m \Big[\Big(\beta_2^{(m)}(\boldsymbol{r}') + \beta_1^{(m)}(\boldsymbol{r}') \Big) \cos 2\theta_0^{(m)} \\
&\qquad + \beta_3^{(m)}(\boldsymbol{r}') \sin 2\theta_0^{(m)} \Big] \qquad \text{(A4)}
\end{aligned}
$$

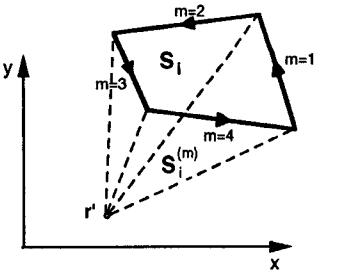

(a)

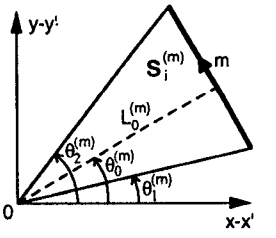

(b)

Fig. 7. (a) The observation cell S_i is divided into a finite number of oriented triangles. (b) Relevant parameters of the oriented triangle $S_i^{(m)}$ in the $(x-x', y-y')$ coordinate system.

with

$$\beta_1^{(m)}(\boldsymbol{r}') = -\frac{1}{L_0^{(m)}} \cdot \left[\sin\left(\theta_2^{(m)} - \theta_0^{(m)}\right) - \sin\left(\theta_1^{(m)} - \theta_0^{(m)}\right)\right]$$

$$\beta_2^{(m)}(\boldsymbol{r}') = \frac{2}{3L_0^{(m)}} \cdot \left[\sin^3\left(\theta_2^{(m)} - \theta_0^{(m)}\right) - \sin^3\left(\theta_1^{(m)} - \theta_0^{(m)}\right)\right]$$

$$\beta_3^{(m)}(\boldsymbol{r}') = \frac{2}{3L_0^{(m)}} \cdot \left[\cos^3\left(\theta_2^{(m)} - \theta_0^{(m)}\right) - \cos^3\left(\theta_1^{(m)} - \theta_0^{(m)}\right)\right]. \quad \text{(A5)}$$

ACKNOWLEDGMENT

The first author is a Research Associate, the last one a Research Director of the National Fund for Scientific Research of Belgium.

REFERENCES

[1] J. Meixner, "The behavior of electromagnetic fields at edges," *IEEE Trans. Antennas Propagat.*, vol. AP-20, pp. 442–446, July 1972.

[2] P. B. Katehi and N. G. Alexopoulos, "Frequency-dependent characteristics of microstrip discontinuities in millimeter-wave integrated circuits," *IEEE Trans. Microwave Theory Tech.*, vol. MTT-33, pp. 1029–1035, Oct. 1985.

[3] J. C. Rautio and R. F. Harrington, "An electromagnetic time-harmonic analysis of shielded microstrip circuits," *IEEE Trans. Microwave Theory Tech.*, vol. MTT-35, pp. 726–730, Aug. 1987.

[4] J. R. Mosig, "Arbitrarily shaped microstrip structures and their analysis with a mixed potential integral equation," *IEEE Trans. Microwave Theory Tech.*, vol. 36, pp. 314–323, Feb. 1988.

[5] N. Faché and D. De Zutter, "Rigorous full-wave space-domain solution for dispersive microstrip lines," *IEEE Trans. Microwave Theory Tech.*, vol. 36, pp. 731–737, Apr. 1988.

[6] L. Beyne and D. De Zutter, "Green's function for layered lossy media with special application to microstrip antennas," *IEEE Trans. Microwave Theory Tech.*, vol. 36, pp. 875–881, May 1988.

[7] X. Zhang and K. K. Mei, "Time-domain finite difference approach to the calculation of the frequency-dependent characteristics of microstrip discontinuities," *IEEE Trans. Microwave Theory Tech.*, vol. 36, pp. 1775–1787, Dec. 1988.

[8] R. W. Jackson, "Full-wave, finite element analysis of irregular microstrip discontinuities," *IEEE Trans. Microwave Theory Tech.*, vol. 37, pp. 81–89, Jan. 1989.

[9] W. P. Harokopus Jr. and P. B. Katehi, "Characterization of microstrip discontinuities on multilayer dielectric substrates including radiation losses," *IEEE Trans. Microwave Theory Tech.*, vol. 37, pp. 2058–2066, Dec. 1989.

[10] W. Wertgen and R. H. Jansen, "Efficient direct and iterative electrodynamic analysis of geometrically complex MIC and MMIC structures," *Int. J. Numerical Modelling: Electronic Networks, Devices and Fields*, vol. 2, pp. 153–186, 1989.

[11] D. M. Sheen, S. M. Ali, M. D. Abouzahra, and J. A. Kong, "Application of the three-dimensional finite-difference time-domain method to the analysis of planar microstrip circuits," *IEEE Trans. Microwave Theory Tech.*, vol. 38, July 1990.

[12] S. C. Wu, H. Y. Yang, N. G. Alexopoulos and I. Wolff, "A rigorous dispersive characterization of microstrip cross and T junctions," *IEEE Trans. Microwave Theory Tech.*, vol. 38, pp. 1837–1843, Dec. 1990.

[13] A. Hill and V. K. Tripathi, "An efficient algorithm for the three-dimensional analysis of passive microstrip components and discontinuities for microwave and millimeter-wave integrated circuits," *IEEE Trans. Microwave Theory Tech.*, vol. 39, pp. 83–91, Jan. 1991.

[14] N. Feix, M. Lalande, and B. Jecko, "Characterization of a microstrip bend by a time frequency method," *IEEE Trans. Microwave Theory Tech.*, to be published in.

[15] J. Sercu, N. Faché, F. Libbrecht, and D. De Zutter, "A full wave space domain analysis technique of open microstrip planar circuits, " in *1992 IEEE AP-S Symp. Dig.*, pp. 1649–1652.

[16] E. Hamerstad and O. Jensen, "Accurate models for microstrip computer-aided design," in *1980 IEEE MTT-S Symp. Dig.*, pp. 407–409

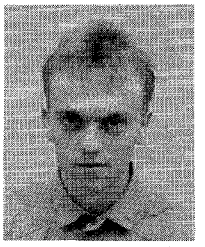

Jeannick Sercu was born in Ieper, Belgium, on February 9, 1967. He received a degree in electrical engineering from the University of Ghent in July 1990. He is currently working toward the Ph.D. degree in electrical engineering at the University of Ghent. His work is sponsored by the National Fund for Scientific Research of Belgium. His research concerns the electromagnetic modeling of microwave planar structures.

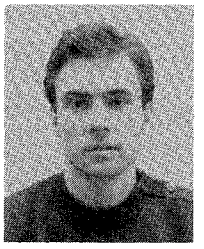

Niels Faché was born in Ghent, Belgium, on July 4, 1964. He received the degree in electrical engineering from the University of Ghent in 1986. In December 1989 he obtained the Ph.D. degree from the Laboratory of Electromagnetism and Acoustics (LEA) at the same University. His research dealt with the full-wave analysis and circuit modeling of two-dimensional electrical interconnections embedded in multilayered media.

In 1990 he worked as a consultant from LEA to the Network Measurements Division (Santa Rosa, CA) of Hewlett-Packard (HP). While at HP, he worked on the improvement of linear models in the Microwave Design System (MDS) and the implementation of new linear models. Currently he is back at LEA where his research now focuses on electromagnetic field solvers and their use in circuit simulators.

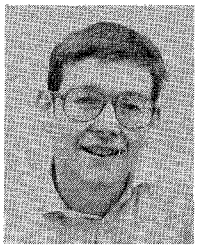

Frank Libbrecht was born in Kortrijk, Belgium, on September 28, 1964. He received the degree in electrical engineering from the University of Ghent in July 1987. He obtained the Ph.D. degree at the same University in 1991 for his research on optical transmission of information. His research now focuses on electromagnetic simulation of microwave planar structures.

Daniël De Zutter (M'92) was born in Eeklo, Belgium, on November 8, 1953. He received a degree in electrical engineering from the University of Ghent in July 1976. From September 1976 to September 1984 he was a research and teaching assistant in the Laboratory of Electromagnetism and Acoustics (LEA) at the same university. In October 1981, he obtained the Ph.D. degree at the University of Ghent and in the spring of 1984 he completed a thesis leading to a degree equivalent to the French Aggrégation or the German Habilitation. He is now a professor at Ghent University and Research Director at the National Science Foundation of Belgium.

Most of his earlier scientific work dealt with the electrodynamics of moving media, with emphasis on the Doppler effect and Lorentz forces. His research now focuses on all aspects of circuit and electromagnetic modelling of high-speed and high-frequency interconnections and on EMC and EMI topics. He has contributed to more than 30 journal papers and about 40 conference papers. In 1990 he was elected Member of the Electromagnetics Society.